arXiv:1604.08384v1 [cond-mat.str-el] 28 Apr 2016

Tuning towards dynamic freezing using a two-rate protocol

Satyaki Kar, Bhaskar Mukherjee, and K. Sengupta
Theoretical Physics Department, Indian Association for the Cultivation of Science, Jadavpur, Kolkata-700032, India.
(Dated: April 29, 2016)

We study periodically driven closed quantum systems where two parameters of the system Hamiltonian are driven with frequencies ω_1 and $\omega_2 = r\omega_1$. We show that such drives may be used to tune towards dynamics induced freezing where the wavefunction of the state of the system after a drive cycle at time $T = 2\pi/\omega_1$ has almost perfect overlap with the initial state. We locate regions in the (ω_1, r) plane where the freezing is near exact for a class of integrable and a specific non-integrable model. The integrable models that we study encompass Ising and XY models in $d = 1$, Kitaev model in $d = 2$, and Dirac fermions in graphene and atop a topological insulator surface whereas the non-integrable model studied involves the experimentally realized one-dimensional (1D) tilted Bose-Hubbard model in an optical lattice. In addition, we compute the relevant correlation functions of such driven systems and describe their characteristics in the region of (ω_1, r) plane where the freezing is near-exact. We supplement our numerical analysis with semi-analytic results for integrable driven systems within adiabatic-impulse approximation and discuss experiments which may test our theory.

PACS numbers: 73.43.Nq, 05.70.Jk, 64.60.Ht, 75.10.Jm

I. INTRODUCTION

The behavior of closed quantum systems driven out of equilibrium has attracted a lot of attention in recent times[1–3]. Such out-of-equilibrium systems explore a major region (if not all) of it's Hilbert space leading to a gamut of novel phenomena which have no equilibrium counterparts. For example, they exhibit universal scaling of excitation density when driven slowly through a quantum critical point[4–9]. Another such class of phenomenon involves dynamic transition where the free energy density of a quantum system after a quench develops non-analyticities leading to sharp cusp-like features in it's Lochsmidt echo pattern at specific times[10–14]; these transitions have no equilibrium analogs and can not be described by any local order parameter. Furthermore, the universality and the possibility of application of renormalization group (RG) methods to such driven systems has been a subject of recent research[15–17]; such analysis also leads to a several interesting features involving RG flow and universality of driven systems which are qualitatively different from their equilibrium counterparts.

A class of such dynamical phenomenon involve periodically driven quantum systems leading to multiple passages through their critical points during a drive cycle[18–22]. Such systems exhibit a wide class of dynamical phenomena which do not occur in their aperiodically driven counterparts. For example, they display signatures of Stuckelberg interference phenomenon in their excitations densities, dynamical correlation functions, and thermodynamic quantities such as work distribution[20,23]. Furthermore, periodically driven integrable systems show a separate class of dynamical transitions which originates from the change in topology of their Floquet spectrum and leaves its imprint on temporal behavior of local correlation functions[24]. Such driven systems also exhibit the phenomenon of dynamics induced freezing[21,22,25,26]; this phenomenon manifests itself in a near unity overlap of the system wavefunction after single or multiple drive period(s) with the initial wavefunction at $t = 0$. Such near-unity overlap signifying freezing occurs at specific discrete frequencies ω^* and is therefore qualitatively different from the trivial freezing that occurs for ultrafast drive frequencies.

In all of the phenomena mentioned above, the drive protocols used involve quench, ramp, or periodic change of a single parameter of the system Hamiltonian as a function of time. More recently, a separate class of protocols involving linear or power law ramp of two Hamiltonian parameters with distinct rate has been studied in details[22,26,27]. The novel features of dynamics induced by such two-rate ramp protocols include a generalization of the Kibble-Zurek scaling laws and possibility of reduction of excitation production as the system is ramped through a quantum critical point. The latter feature leads to better fidelity for quantum state preparation and provide a controlled way of reduction of heating during dynamics in critical systems[22]. To the best of our knowledge, the study of dynamics of closed quantum critical systems for such two rate protocols has been carried out for ramp protocols only; no such studies have been undertaken for periodic drives.

In this work, we aim to fill up this gap in the literature by studying the effect of two-rate periodic drive protocols on both integrable and non-integrable closed quantum systems. The drive protocol chosen involves periodic variation of two parameters of the system Hamiltonian with frequencies ω_1 and $\omega_2 = r\omega_1$. For integrable models, we choose a class of models represented by free fermionic Hamiltonian $H = \sum_{\vec{k}} \psi^\dagger_{\vec{k}} H_{\vec{k}} \psi_{\vec{k}}$, where $\psi_{\vec{k}} = (c_{\vec{k}}, c^\dagger_{-\vec{k}})^T$ is the two component fermion field, $c_{\vec{k}}$ denotes fermionic annihilation operator, and $H_{\vec{k}}$ is a 2×2 matrix Hamiltonian density given by

$$H_{\vec{k}} = \left[\lambda_1(\omega_1 t) - b_{\vec{k}}\right] \tau_3 + \lambda_2(r\omega_1 t)\Delta_{\vec{k}}\tau_1 \qquad (1)$$

where τ_3 and τ_1 are Pauli matrices in particle-hole space. Such free fermionic Hamiltonians represents Ising and XY models in $d = 1$[28] and Kitaev model in $d = 2$[29–31]. In addition, it also describes Dirac-like quasiparticles in graphene[32] and on the surface of a topological insulators[33]. In what follows we shall carry out numerical analysis of this model in the context of XY model in $d = 1$; we note, however, that our results shall be valid for any other representations of $H_{\vec{k}}$.

The XY model in a transverse field constitute a model for of half-integer spins on a one-dimensional (1D) chain whose Hamiltonian is given by

$$H_{\rm XY} = \sum_{\langle ij\rangle,\alpha=x,y} J_\alpha S_i^\alpha S_j^\alpha - h\sum_i S_i^z, \tag{2}$$

where $J_{x,y}$ are nearest coupling between x and the y components of the spins, $\langle ij\rangle$ indicates that j is one of the neighboring sites of i, and h is the transverse field. A standard Jordan-Wigner transformation[3] maps Eq. 2 to Eq. 1 in $d = 1$ with the identification

$$\begin{aligned} b_k &= (J_x + J_y)\cos(k), \quad \lambda_1 = -h \\ \Delta_k &= -i\sin(k), \quad \lambda_2 = (J_x - J_y) \end{aligned} \tag{3}$$

For non-integrable system, we choose the recently experimentally realized ultracold boson in their Mott insulating phase in the presence of an artificial electric field created either by shifting the center of the confining harmonic trap or by applying the spatially varying Zeeman magnetic field to the spinor bosons[26,34–38]. The Hamiltonian of such bosons can be written as

$$H_1 = -J\sum_{\langle ij\rangle}(b_i^\dagger b_j + \text{h.c}) + \sum_i \left[\frac{U}{2}n_i(n_i-1) - En_i i\right] \tag{4}$$

where b_i denotes boson annihilation operator on site i, U is the on-site interaction, E is the magnitude of the effective electric field in units of energy[34], J is hopping amplitude of bosons between the nearest site, and $n_i = b_i^\dagger b_i$ is the boson number operator. It has been shown in Ref. 34 that the low-energy properties of H_1 is captured by a dipole model whose Hamiltonian is given by

$$H_d = -J\sqrt{n_0(n_0+1)}\sum_\ell (f_\ell^\dagger + f_\ell) + (U-E)\sum_\ell n_\ell, \tag{5}$$

where $f_\ell = b_i^\dagger b_j/\sqrt{n_0(n_0+1)}$ is the dipole annihilation operator living on the link ℓ between sites i and j, and n_0 denotes the boson occupation number of the parent Mott phase. These dipoles constitute bound states of a boson and a hole on adjacent sites i and j of the lattice and $n_\ell = f_\ell^\dagger f_\ell$ is the dipole number operator residing on the link ℓ between these sites. The dipole operators satisfy two additional constraints; first, at most one dipole can occur on any link ($n_\ell \le 1$) and second, the maximal number of dipoles on two adjacent links is also unity ($n_\ell n_{\ell\pm1} = 0$). The model has two ground states; for $U \gg E$, the state correspond to the dipole vacuum which is same as the parent Mott state of the bosons while for $U \ll E$, the state corresponds to maximal number of dipoles which is a density wave state for the bosons. It was shown in Ref. 34 that these two ground states are separated by a transition at $E_c = U + 1.31J\sqrt{n_0(n_0+1)}$ which belongs to the Ising universality class. These phases of the model and the signature of the Ising transition between them have been verified in a recent experiment[38]. The non-equilibrium dynamics of the model for single parameter quench, ramp and periodic protocols have also been studied[26,36,37]. In what follows, we shall vary the electric field E and hopping amplitude J of these models according to periodic protocols characterized by frequencies ω_1 and $\omega_2 = r\omega_1$ respectively.

The main results that we obtain from such a study are the following. First, we develop an analytical framework for studying dynamics for integrable models (Eq. 1) subjected to arbitrary two-rate periodic protocol characterized by frequencies ω_1 and $\omega_2 = r\omega_1$ using an adiabatic-impulse approximation[39]; the formalism developed constitutes a generalization of the adiabatic-impulse approximation method to two-rate periodic protocols. We show that in the low-frequency regime, where this approximation is expected to be accurate, our results match those obtained using exact numerics. Second, we chart out, both numerically and using adiabatic impulse approximation, the overlap between the wavefunctions at the end of a drive period ($T = 2\pi/\omega_1$) and the initial ground state wavefunction as a function of ω_1 and r. Our results demonstrate that the second drive frequency can be used as a tuning parameter to obtain dynamics induced freezing, *i.e.*, a near-perfect overlap between these wavefunctions. In particular, for the integrable models studied here, we show that $r = 1$ seems to be the best choice for obtaining dynamic freezing and provide a semi-analytic explanation of this result. Third, we compute equal-time correlation functions of the XY model as a function of ω_1 and r and discuss the signature of dynamics induced freezing in such correlation functions. Fourth, we study the dynamics of the tilted Bose-Hubbard model driven out of equilibrium via the two-rate protocol described above using exact diagonalization (ED) for finite size systems with $N \le 16$. We show that such a drive leads to near-perfect dynamics induced freezing for several ω_1 for $r = 2$, provide a qualitative explanation of this phenomenon using a numerically supported effective two state model, and compute the dipole-dipole correlation functions which bear the signature of such freezing phenomenon. Finally, we chart our experiments which can be used to test our theory.

The plan of the rest of the paper is as follows. In Sec. II, we analyze the integrable fermionic Hamiltonian (Eq. 1) using both adiabatic-impulse approximation and exact numerics. This is followed by Sec. III, where we study the dynamics of the dipole model (Eq. 5). Finally we summarize our results, discuss their experimental implications, and conclude in Sec. IV.

II. INTEGRABLE MODELS

In this section we shall study the dynamics of the free fermion Hamiltonian given by Eq. 1 subjected to the two rate periodic protocol. We first analyze such dynamics using an adiabatic-impulse approximation in Sec. II A. This is followed by discussion of results from exact numerics in Sec. II B, carried out using appropriate parameters for 1D XY model (Eqs. 2 and 3), and their comparison with those obtained from

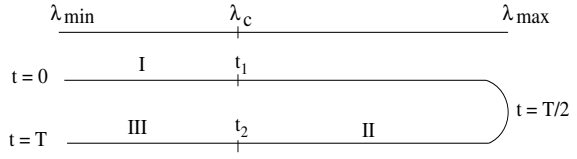

FIG. 1: Schematic representation of the time-evolution of the system with a critical point being located at $\lambda = \lambda_c$, Regions I, II and III are the adiabatic regimes separated by impulse regions at $t = t_1 \equiv t_{1\vec{k}}$ and $t = t_2 \equiv t_{2\vec{k}}$ when the system traverse the critical point. See text for details.

adiabatic-impulse approximation developed in Sec. II A.

A. Adiabatic-Impulse Approximation

The basic assumption behind the adiabatic-impulse approximation lies in dividing the dynamics of a system subjected to a drive into two distinct regimes[39]. The first is the adiabatic regime where the rate at which the system Hamiltonian changes is small compared to the instantaneous energy gap; here the dynamics merely lead to accumulation of a phase of the system wavefunction. The second constitute the impulse regime where the rate of change of the Hamiltonian parameter is comparable to or larger than the instantaneous energy gap; in this regime, excitations are produced since the system can no longer follow the instantaneous ground state. In the context of the Hamiltonian given by Eq. 1, the latter region occurs when the system reaches the critical point. This approximation therefore becomes accurate for low-frequency drives where the impulse regime occurs near the critical point of the Hamiltonian. In what follows, we shall proceed with the assumption that $H_{\vec{k}}$ (Eq. 1) has an isolated critical point which the system crosses during the evolution; this assumption fails when the $H_{\vec{k}}$ has a gapless region such as for the Kitaev model[24,29,31]. In this case, the adiabatic-impulse approximation can not be used in its present form. In this section, we shall only discuss cases where $H_{\vec{k}}$, given by Eq. 1, does not have such gapless regions.

To treat the dynamics of Eq. 1 subjected to a two-rate periodic protocol using the adiabatic-impulse approximation, we first sketch the adiabatic and the impulse regions in Fig. 1. We denote the instantaneous ground state at a given momentum $\vec{k}$ to be the ground sate of the $H_{\vec{k}}(t)$(Eq. 1): $|\psi_{\vec{k}}\rangle_1 = (u^0_{\vec{k}}(t), v^0_{\vec{k}}(t))^T$, where

$$\begin{aligned} u^0_{\vec{k}}(t) &= \frac{\lambda_2(t)\Delta_{\vec{k}}}{D_{\vec{k}}(t)}, \quad v^0_{\vec{k}}(t) = -\frac{(\lambda_1(t) - b_{\vec{k}}) + E_{\vec{k}}(t)}{D_{\vec{k}}(t)} \\ E_{\vec{k}}(t) &= \sqrt{(\lambda_1(t) - b_{\vec{k}})^2 + \lambda_2^2(t)\Delta^2_{\vec{k}}} \\ D_{\vec{k}}(t) &= \sqrt{(\lambda_1(t) - b_{\vec{k}} + E_{\vec{k}}(t))^2 + \lambda_2^2(t)\Delta^2_{\vec{k}}} \end{aligned} \tag{6}$$

The corresponding instantaneous excited state wavefunction for any given $\vec{k}$ is given by $|\psi_{\vec{k}}(t)\rangle_2 = (-v^0_{\vec{k}}(t), u^0_{\vec{k}}(t))^T$. Using Eq. 6, one can write down the wavefunction of the driven system at any time t and for a given $\vec{k}$ as

$$|\psi_{\vec{k}}(t)\rangle = b'_{1\vec{k}}(t)|\psi_{\vec{k}}(t)\rangle_1 + b'_{2\vec{k}}(t)|\psi_{\vec{k}}(t)\rangle_2 \tag{7}$$

with $(b'_{1\vec{k}}(0), b'_{2\vec{k}}(0)) = (1, 0)$. In what follows, we shall use the notation $u_{\vec{k}}(0) = u^0_{\vec{k}}(T) \equiv u^0_{\vec{k}}$ and $v_{\vec{k}}(0) = v^0_{\vec{k}}(T) \equiv v^0_{\vec{k}}$.

To obtain expressions for $b'_{1,2\vec{k}}(t)$, we first identify the times $t_{1\vec{k}}$ and $t_{2\vec{k}}$ (Fig. 1) at which the system comes to an avoided level crossing for a given momenta $\vec{k}$. To this end, we note that the instantaneous energy gap of the system is given by

$$\delta E_{\vec{k}} = 2\sqrt{(\lambda_1(\omega_1 t) - b_{\vec{k}})^2 + \lambda_2^2(r\omega_1 t)\Delta^2_{\vec{k}}}. \tag{8}$$

This gap reaches a minima at $t = t_{1,2\vec{k}}$ at an avoided level crossing for which $\partial \delta E_{\vec{k}}/\partial t = 0$. This leads to

$$\dot{\lambda}_1(\omega_1 t_{1\vec{k}})\left[\lambda_1(\omega_1 t_{1\vec{k}}) - b_{\vec{k}}\right] + \dot{\lambda}_2(\omega_2 t_{1\vec{k}})\lambda_2(\omega_2 t_{1\vec{k}})\Delta^2_{\vec{k}} = 0, \tag{9}$$

where $\dot{x} = \partial_t x$. For simple enough protocols, it is possible to solve this equation to obtain an analytic expression for $t_{1,2\vec{k}}$. For example if $\lambda_1 = \lambda_2 = A\cos(\omega_1 t)$, one obtains $\omega_1 t_{1\vec{k}} = \arccos[Ab_{\vec{k}}/(A^2 + \Delta^2_{\vec{k}})]$ and $\omega_1 t_{2\vec{k}} = 2\pi - \omega_1 t_{1\vec{k}}$. In other, more complicated cases, one needs to solve Eq. 9 numerically to obtain $t_{1,2\vec{k}}$.

Let us now consider the evolution of the system in region I (Fig. 1) for $t < t_{1\vec{k}}$. In this region, the system is in the adiabatic regime and the wavefunction merely gathers a kinetic phase during evolution. The evolution operator in this regime is thus given by[39]

$$U_1(t, 0) = e^{-i\Omega_{1\vec{k}}(t)\tau_3}, \ \Omega_{1\vec{k}}(t) = \frac{1}{2}\int_0^t \delta E_{\vec{k}}(t')dt' \tag{10}$$

Similarly, in region II for $t_{1\vec{k}} < t < t_{2\vec{k}}$ and III, for $t_{2\vec{k}} < t \leq T$, the evolution operators are given by

$$\begin{aligned} U_2(t, t_{1\vec{k}}) &= e^{-i\Omega_{2\vec{k}}(t)\tau_3}, \ \Omega_{2\vec{k}}(t) = \frac{1}{2}\int_{t_{1\vec{k}}}^t \delta E_{\vec{k}}(t')dt' \\ U_3(t, t_{2\vec{k}}) &= e^{-i\Omega_{3\vec{k}}(t)\tau_3}, \ \Omega_{3\vec{k}}(t) = \frac{1}{2}\int_{t_{2\vec{k}}}^t \delta E_{\vec{k}}(t')dt' \end{aligned} \tag{11}$$

Around $t = t_{1,2\vec{k}}$, the system enters the impulse regions and excitations are produced. The key aspect of the adiabatic-impulse approximation is to approximate the impulse region to be exactly at $t_{1,2,\vec{k}}$. Near these points, the effective Hamiltonian has the form

$$\begin{aligned} \mathcal{H}^a_{\vec{k}}(t) &= \left[\Lambda_{1\vec{k}} + \dot{\lambda}_1(\omega_1 t_{a\vec{k}})\delta t_{a\vec{k}}\right]\tau_3 \\ &\quad + \left[\Lambda_{2\vec{k}} + \dot{\lambda}_2(\omega_2 t_{a\vec{k}})\delta t_{a\vec{k}}\Delta_{\vec{k}}\right]\tau_1 \\ \Lambda_{1\vec{k}} &= \lambda_1(\omega_1 t_{a\vec{k}}) - b_{\vec{k}} \\ \Lambda_{2\vec{k}} &= \Delta_{\vec{k}}\lambda_2(\omega_2 t_{a\vec{k}}), \quad \delta t_{a\vec{k}} = t - t_{a\vec{k}}, \end{aligned} \tag{12}$$

where $a = 1, 2$ for the two impulse regions. We note that in contrast to standard applications[23,39], the impulse Hamiltonian $\mathcal{H}_{\vec{k}}$ for the two-rate protocol is not of the Landau-Zener form; in contrast, it has time-dependence both in the diagonal and off-diagonal terms. To apply the Landau-Zener result, we therefore cast it in the standard form following the method suggested in Ref. 27. To this end, we first write $\mathcal{H}_{\vec{k}}(t)$ in terms of a new set of Pauli matrices as

$$\mathcal{H}^a_{\vec{k}}(t) = \mu^a_{1\vec{k}}(\delta t_{a\vec{k}} - t'_{a\vec{k}})\tilde{\tau}_3 + \mu^a_{2\vec{k}}\tilde{\tau}_1 \quad (13)$$

A comparison of Eqs. 12 and 13 shows that for both equations to be simultaneously correct, one needs

$$\begin{aligned}\tilde{\tau}_3\mu^a_{1\vec{k}} &= \dot{\lambda}_1(\omega_1 t_{a\vec{k}})\tau_3 + \dot{\lambda}_2(\omega_2 t_{a\vec{k}})\Delta_{\vec{k}}\tau_1 \\ \tilde{\tau}_1\mu^a_{2\vec{k}} &= (\Lambda_{1\vec{k}} + \dot{\lambda}_1(\omega_1 t_{a\vec{k}})t'_{a\vec{k}})\tau_3 \\ &\quad +(\Lambda_{2\vec{k}} + \dot{\lambda}_2(\omega_2 t_{a\vec{k}})t'_{a\vec{k}}\Delta_{\vec{k}})\tau_1 \end{aligned} \quad (14)$$

The identities $(\mathrm{Det}[\tilde{\tau}_{1,3}])^2 = 1$ and $\{\tilde{\tau}_3, \tilde{\tau}_1\} = 0$, then leads to

$$\begin{aligned}\mu^a_{1\vec{k}} &= \sqrt{\dot{\lambda}_1^2(\omega_1 t_{a\vec{k}}) + \dot{\lambda}_2^2(\omega_2 t_{a\vec{k}})\Delta^2_{\vec{k}}} \\ \mu^a_{2\vec{k}} &= \Big[(\Lambda_{1\vec{k}} + \dot{\lambda}_1(\omega_1 t_{a\vec{k}})t'_{a\vec{k}})^2 \\ &\quad +(\Lambda_{2\vec{k}} + \dot{\lambda}_2(\omega_2 t_{a\vec{k}})t'_{a\vec{k}}\Delta_{\vec{k}})^2\Big]^{1/2} \\ t'_{a\vec{k}} &= -(\dot{\lambda}_1(\omega_1 t_{a\vec{k}})\Lambda_{1\vec{k}} + \dot{\lambda}_2(\omega_2 t_{a\vec{k}})\Lambda_{2\vec{k}})/\mu^2_{1\vec{k}}. \end{aligned} \quad (15)$$

For the Hamiltonian given by Eqs. 13 and 15, the probability of excitation production can be read off as[1]

$$p^a_{\vec{k}} = \exp[-2\pi\delta^a_{\vec{k}}], \quad \delta^a_{\vec{k}} = |\mu^a_{2\vec{k}}|^2/\left(2|\mu^a_{1\vec{k}}|\right) \quad (16)$$

Using Eq. 16, one can write down the unitary evolution matrices Σ_a which propagates the wavefunction across $t = t_{a\vec{k}}$[39]. The elements of Σ_a can be expressed in terms of $p^a_{\vec{k}}$ and the Stokes phase $\tilde{\phi}^a_{s\vec{k}}$ as

$$\begin{aligned}\Sigma_a &= \begin{pmatrix} \sqrt{1-p^a_{\vec{k}}}e^{-i\tilde{\phi}^a_{s\vec{k}}} & -\sqrt{p^a_{\vec{k}}} \\ \sqrt{p^a_{\vec{k}}} & \sqrt{1-p^a_{\vec{k}}}e^{i\tilde{\phi}^a_{s\vec{k}}} \end{pmatrix}, \\ \tilde{\phi}^a_{s\vec{k}} &= -\frac{\pi}{4} + \delta^a_{\vec{k}}\left(\ln\delta^a_{\vec{k}} - 1\right) + \mathrm{Arg}\Gamma\left(1 - i\delta^a_{\vec{k}}\right) \end{aligned} \quad (17)$$

where Γ denotes the gamma function. Using Eqs. 10, 11, and 17, we finally obtain

$$\begin{aligned}\begin{pmatrix} b'_{1\vec{k}} \\ b'_{2\vec{k}} \end{pmatrix} &= U_3(T, t_{2\vec{k}})\,\Sigma^2_{\vec{k}}\,U_2(t_{2\vec{k}}, t_{1\vec{k}})\,\Sigma^1_{\vec{k}}\,U_1(t_{1\vec{k}}, 0)\begin{pmatrix} 1 \\ 0 \end{pmatrix} \\ &= \begin{pmatrix} q_{+\vec{k}} & -q^*_{-\vec{k}} \\ q_{-\vec{k}} & q^*_{+\vec{k}} \end{pmatrix}\begin{pmatrix} 1 \\ 0 \end{pmatrix} = \begin{pmatrix} q_{+\vec{k}} \\ q_{-\vec{k}} \end{pmatrix} \\ q_{+\vec{k}} &= e^{-i\Omega_{3\vec{k}}}\Big[\sqrt{(1-p^1_{\vec{k}})(1-p^2_{\vec{k}})}e^{-i\sum_{a=1}^2(\Omega_{a\vec{k}}+\tilde{\phi}^a_{s\vec{k}})} \\ &\quad -\sqrt{p^1_{\vec{k}}p^2_{\vec{k}}}e^{i(\Omega_{2\vec{k}}-\Omega_{1\vec{k}})}\Big] \\ q_{-\vec{k}} &= e^{i\Omega_{3\vec{k}}}\Big[\sqrt{(1-p^2_{\vec{k}})p^1_{\vec{k}}}e^{i(\tilde{\phi}^2_{s\vec{k}}+\Omega_{2\vec{k}}-\Omega_{1\vec{k}})} \\ &\quad +\sqrt{(1-p^1_{\vec{k}})p^2_{\vec{k}}}e^{-i(\tilde{\phi}^1_{s\vec{k}}+\Omega_{1\vec{k}}+\Omega_{2\vec{k}})}\Big] \\ |\psi_{\vec{k}}(T)\rangle &= \begin{pmatrix} q_{+\vec{k}}u^0_{\vec{k}} - q_{-\vec{k}}v^0_{\vec{k}} \\ q_{+\vec{k}}v^0_{\vec{k}} + q_{-\vec{k}}u^0_{\vec{k}} \end{pmatrix} = \begin{pmatrix} u_{\vec{k}}(T) \\ v_{\vec{k}}(T) \end{pmatrix} \end{aligned} \quad (18)$$

Eq. 18 is the central result of this section. It allows us to express the final wavefunction at the end of a drive period for an arbitrary two-rate drive protocol. We note that the expressions of $q_{\pm\vec{k}}$ obtained in Eq. 18 constitutes a generalization of its single-rate protocol counterpart[39]. Furthermore, it allows us to obtain semi-analytic expressions for excitation density and all fermionic correlators at the end of the drive. In the context of XY model in a transverse field where the transverse spin correlators can be expressed in terms of fermionic correlators[34], Eq. 18 allows us to obtain analytic expressions for the transverse magnetization and other relevant spin correlation functions. In what follows, we shall be interested in equal-time fermionic correlation functions

$$\begin{aligned}C_{\vec{i}-\vec{j}} &= L^{-d}\sum_{\vec{k}}\langle\psi_{\vec{k}}(T)|(c^\dagger_{\vec{k}}c_{\vec{k}} + \mathrm{h.c.})|\psi_{\vec{k}}(T)\rangle \\ &\quad \times\cos[\vec{k}\cdot(\vec{i}-\vec{j})] \\ &= L^{-d}\sum_{\vec{k}}|v_{\vec{k}}(T)|^2\cos[\vec{k}\cdot(\vec{i}-\vec{j})] \\ F_{\vec{i}-\vec{j}} &= L^{-d}\sum_{\vec{k}}\langle\psi_{\vec{k}}(T)|(c_k c_{-k} + \mathrm{h.c.})|\psi_{\vec{k}}(T)\rangle \\ &\quad \times\sin[\vec{k}\cdot(\vec{i}-\vec{j})] \\ &= L^{-d}\sum_{\vec{k}}(u^*_{\vec{k}}(T)v_{\vec{k}}(T) + \mathrm{h.c.})\sin[\vec{k}\cdot(\vec{i}-\vec{j})] \end{aligned} \quad (19)$$

and the excitation density n_d

$$n_d = 1 - F, \quad F = L^{-d}\sum_{\vec{k}}|\langle\psi^0_{\vec{k}}|\psi_{\vec{k}}(T)\rangle|^2 \quad (20)$$

where F is the wavefunction overlap at the end of the drive which approaches close to unity for dynamics induced freezing, the sum over momenta extends over half of the Brillouin zone, and L is the linear dimension of the system. These quantities can be expressed in terms of $q_{\pm\vec{k}}$ and the instantaneous eignstates at $t = T$, $u^0_{\vec{k}}$ and $v^0_{\vec{k}}$, using Eqs. 18 and 7, as

$$\begin{aligned}n_d &= 1 - F = L^{-d}\sum_{\vec{k}}|q_{-\vec{k}}|^2 \quad (21) \\ C_{\vec{i}-\vec{j}} &= L^{-d}\sum_{\vec{k}}|q_{-\vec{k}}u^0_{\vec{k}} + q_{+\vec{k}}v^0_{\vec{k}}|^2\cos[\vec{k}\cdot(\vec{i}-\vec{j})] \\ F_{\vec{i}-\vec{j}} &= L^{-d}\sum_{\vec{k}}\Big[\left(q^*_{+\vec{k}}u^0_{\vec{k}} - q^*_{-\vec{k}}v^0_{\vec{k}}\right)\left(q_{-\vec{k}}u^0_{\vec{k}} + q_{+\vec{k}}v^0_{\vec{k}}\right) \\ &\quad +\mathrm{h.c.}\Big]\sin[\vec{k}\cdot(\vec{i}-\vec{j})] \quad (22) \end{aligned}$$

In the next section, we shall use Eq. 22 to discuss the behav-

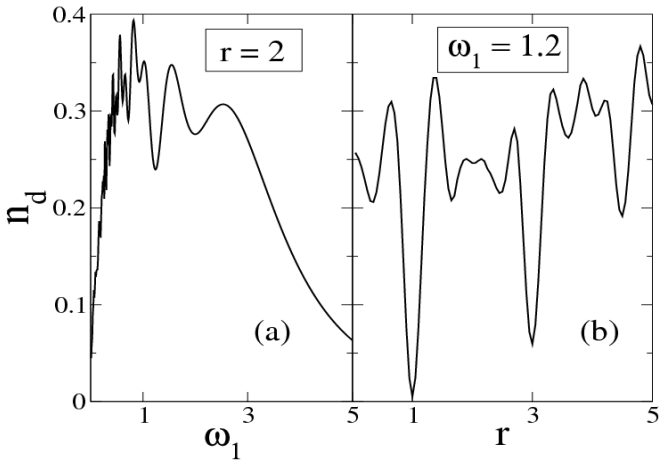

FIG. 2: (a) Plot of the defect density n_d of the 1D XY model in a transverse field as a function of the drive frequency ω_1 for $r = 2$. Here we have chosen $J_x + J_y = 1$, $J_x - J_y = \cos(r\omega_1 t + \phi)$, and $h = A\cos(\omega_1 t)$ with $A = 4$ and $\phi = 0$. (b) Plot of n_d as a function of r for $\omega_1 = 1.2$ and with all parameters same is (a). Note that $r = 0$ correspond to the single parameter drive protocol. A clear signature of dynamic freezing is found at $r = 1$ and $\omega_1 = 1.2$.

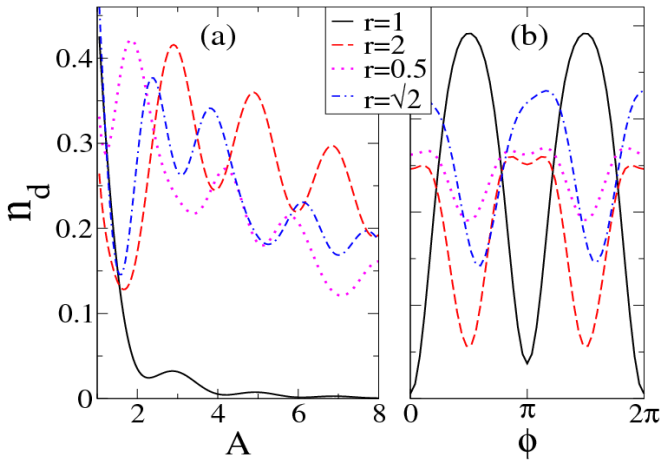

FIG. 3: (a) Variation of the defect density n_d as a function of the drive amplitude for $\omega_1 = 1.2$, $\phi = 0$, and several representative values of r. All other parameters are same in Fig. 2. (b) Variation of n_d as a function of the initial phase ϕ of the drive for $A = 4$.

ior of magnetization, excitation density and correlation functions of the transverse field XY models as computed using adiabatic-impulse technique and compare with the exact numerics.

B. Results for integrable models

In this section, we discuss numerical results obtained by exact numerical solution of the driven Hamiltonian Eq. 1 and compare those obtained Sec. II A using generalized adiabatic-impulse approximation. To do this, we take advantage of the fact that H_k represents a two-level Hamiltonian for each $(\vec{k}, -\vec{k})$ pair. Thus for every given $\vec{k}$, it is possible to write a wavefunction $|\psi_{\vec{k}}(t)\rangle = (u_{\vec{k}}(t), v_{\vec{k}}(t))^T$ which satisfies

$$\begin{aligned} i\partial_t u_{\vec{k}}(t) &= (\lambda_1(t) - b_{\vec{k}})u_{\vec{k}}(t) + \lambda_2(t)\Delta_{\vec{k}} v_{\vec{k}}(t) \\ i\partial_t v_{\vec{k}}(t) &= -(\lambda_1(t) - b_{\vec{k}})v_{\vec{k}}(t) + \lambda_2(t)\Delta_{\vec{k}} u_{\vec{k}}(t), \end{aligned} \quad (23)$$

where we first choose the parameters $\lambda_{1(2)}(t)$, $b_{\vec{k}}$, and $\Delta_{\vec{k}}$ to be those for XY model in a transverse field (Eq. 3) with $\lambda_1 = A\cos(\omega_1 t)$, $\lambda_2 = \cos(r\omega_1 t + \phi)$, and $J_{x(y)} = (1 + (-)\lambda_2(t))/2$. Note that our choice of parameters is equivalent to scaling all energy parameters of the Hamiltonian with $J_x + J_y$ and all time scales with $\hbar/(J_x + J_y)$. A numerical solution of Eq. 23 enables us to obtain $|\psi_k(t)\rangle$ which leads to the defect density n_d and the correlation functions C_{ij} and F_{ij} using Eqs. 20 and 19 at the end of a single drive period $T = 2\pi/\omega_1$.

The results of the numerical procedure described above is shown in Figs. 2, 3, and 4. In Fig. 2(a), we plot n_d as a function of ω_1 for $r = 2$ while in Fig. 2(b), we plot n_d as a function of r for $\omega_1 = 1.2$. These plots clearly demonstrate that n_d approaches zero close to $r = 1$ and $\omega_1 = 1.2$; at this point, $|\psi_{\vec{k}}(T)\rangle$ has almost perfect overlap with $|\psi_k(0)\rangle$ for all k which signifies dynamic freezing. We note that such a freezing does not occur for a single parameter drive protocol (which corresponds to $r = 0$) for any ω_1; thus our results demonstrate that the second drive frequency, or equivalently r, for a two-parameter drive protocol can act as a tuning parameter to obtain such freezing. A plot of n_d as a function of the drive amplitude A (Fig 3(a)) and the initial phase ϕ (Fig 3(b)) for several representative values of r indicates that n_d indeed reaches a minimum of $r = 1$ for all $A > 1$; n_d decreases rapidly with increasing A for $r = 1$ while it displays a slow oscillatory decay for other values of r. Further n_d reaches a minimal value for $\phi = 0$ as shown in Fig. 3(b). A comparison of these exact numerical results with those obtained using adiabatic-impulse approximation (Eq. 21) for n_d is shown in Fig. 4. We find that the adiabatic-impulse approximation turns out to match the exact numerical results for n_d for all $\omega_1 \leq 1$ and for any r.

From Figs. 2, 3, and 4, it becomes apparent that the dynamics of $r = 1$ is qualitatively different from that at $r \neq 1$ since it shows a rapid decay of n with both ω_1 and A. We now present a reason for this behavior. We first note that at $r = 1$, the dynamics is controlled by $H_{\vec{k}}^{r=1}$ given by

$$H_{\vec{k}}^{r=1} = \left(Af(\omega_1 t) - b_{\vec{k}}\right)\tau_3 + \Delta_{\vec{k}} f(\omega_1 t)\tau_1, \quad (24)$$

where we have chosen $f(\omega_1 t) = \cos(\omega_1 t)$ for Figs. 2..4. It turns out that $H_{\vec{k}}^{r=1}$ can be cast onto a form[27]

$$H_{\vec{k}}^{r=1} = \alpha_{\vec{k}}(f(\omega_1 t) - t_{1\vec{k}})\tilde{\tau}_3 + \alpha_{2\vec{k}}\tilde{\tau}_1 \quad (25)$$

where $\tilde{\tau}_{1,3}$ are new Pauli matrices which are related to $\tau_{1,3}$ by

$$\begin{aligned} \alpha_{1\vec{k}}\tilde{\tau}_3 &= A\tau_3 + \Delta_{\vec{k}}\tau_1 \\ \alpha_{2\vec{k}}\tilde{\tau}_1 &= (At_{1\vec{k}} - b_{\vec{k}})\tau_3 + \Delta_{\vec{k}} t_{1\vec{k}}\tau_1. \end{aligned} \quad (26)$$

Using the properties that $\mathrm{Det}\tilde{\tau}_{1,3} = -1$ and $\{\tau_3, \tau_1\}_+ = 0$

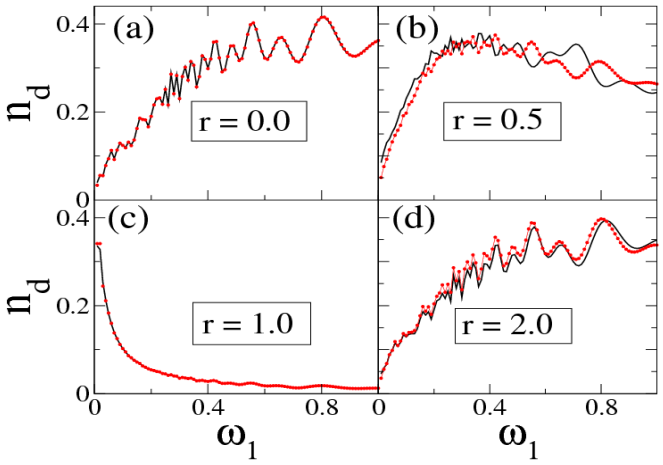

FIG. 4: Comparison of exact numerical result (black solid line) for variation of n_d as a function of ω_1 with that obtained from the adiabatic-impulse method (red dotted line) detailed in Sec. II A for (a) $r = 0$, (b) r=0.5, (c) $r = 1$ and (d) $r = 2$. All parameters are same as in Fig. 2.

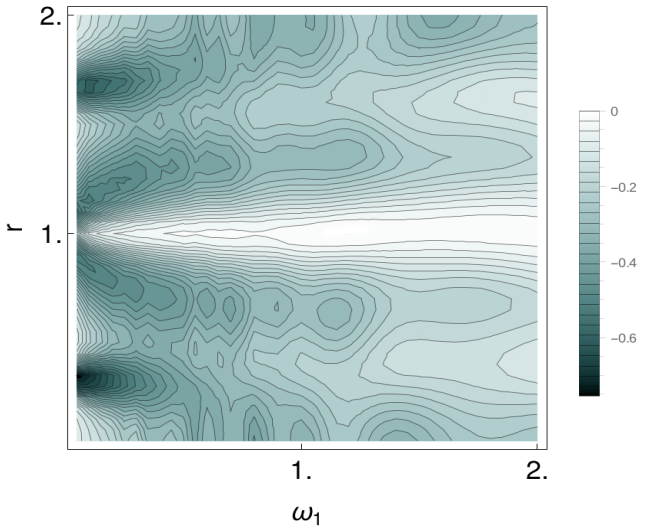

FIG. 5: Plot of the transverse magnetization $\delta m_z = m_z(T) - m_z(0)$ as a function of r and ω_1. The dark patch at $r = 1$ is a signature of the dynamical freezing phenomenon which leads to $\delta m_z = 0$.

(where $\{..\}_+$ denotes anticommutator) one obtains

$$\begin{aligned} \alpha_{1\vec{k}} &= -\sqrt{A^2 + \Delta_{\vec{k}}^2} \\ t_{1\vec{k}} &= A b_{\vec{k}}/\alpha_{1\vec{k}}^2, \quad \alpha_{2\vec{k}} = -\Delta_{\vec{k}} b_{\vec{k}}/\alpha_{1\vec{k}} \end{aligned} \tag{27}$$

We note that such a transformation allows us to write $H_{\vec{k}}$ in terms of new Pauli matrices and with all time dependence being shifted to the diagonal term; such transformation exist for non-linear drive protocols only for $r = 1$, *i.e.*, when the off-diagonal and the diagonal terms of $H_{\vec{k}}^{r=1}$ are driven by identical drive protocol. The avoided level crossings occur at $t = t_{0\vec{k}}$ and $t = T - t_{0\vec{k}}$ where $f(\omega_1 t_0) = b_{\vec{k}}$. Linearizing $H_{\vec{k}}^{r=1}$ around these point, we find that within adiabatic-impulse approximation, the Landau-Zener transition probability $p_{\vec{k}}$ can be read-off from Eq. 25 to be

$$p_{\vec{k}} = e^{-\pi |\alpha_{2\vec{k}}|^2/|\alpha_{1\vec{k}} \dot{f}(\omega_1 t_{0\vec{k}})|} \tag{28}$$

We note that the maximal excitation production occurs from modes around $\vec{k} = \vec{k}_0$. Assuming that $\Delta_{\vec{k}} \sim |\vec{k} - \vec{k}_0|^z$ around $\vec{k}_0$ and $b_{\vec{k}_0} \neq 0$, we find that for $f_1(\omega_1 t) = \cos(\omega_1 t)$

$$p_{\vec{k}} \simeq e^{-b_{\vec{k}}^2 |\vec{k} - \vec{k}_0|^{2z}/(\omega_1 A^3 |\sqrt{1 - b_{\vec{k}}^2/A^2}|)} \tag{29}$$

From Eq. 29 we find that $p_k \to 1$ as A or ω_1 increases; thus the excitation probability after one cycle of the drive $P_{\vec{k}} \sim p_{\vec{k}}(1 - p_{\vec{k}})$ rapidly decays to zero with increasing A or ω_1. It is instructive to compare this decay to the $r = 0$ case where the off-diagonal term in time-independent. In this case one can read off $p_{\vec{k}}$ using the standard results provided in Ref. 39: $p_{\vec{k}}(r = 0) = \exp[-|\vec{k} - \vec{k}_0|^{2z}/(\omega_1 A |\sqrt{1 - b_{\vec{k}}^2/A^2}|)]$. Thus we find $p_{\vec{k}}$ approaches unity with increasing drive amplitude much more rapidly for $r = 1$ which explains the almost monotonic decay of $P_{\vec{k}}$ and hence n_d for $r = 1$.

Finally we plot the change in transverse magnetization at $t = T$, $\delta m_z(T) = m_z(T) - m_z(0)$ for the XY model as a function of r and ω_1 in Fig. 5. We note that this magnetization can be easily obtained from the expressions of the correlation function $C_{\vec{i}-\vec{j}}$ given in Eq. 19

$$m_z(T) = 2L^{-d} \sum_{\vec{k}} |v_{\vec{k}}(T)|^2 - 1 = 2C_0(T) - 1. \tag{30}$$

We note δm_z vanishes if dynamic freezing occurs; such a vanishing of δm_z is clearly seen along the $r = 1$ line in Fig. 5.

III. TITLED BOSE-HUBBARD MODEL

In this section, we shall study the two-rate periodic drive protocol for the tilted Bose-Hubbard model whose Hamiltonian is given by Eq. 4. We shall analyze the dynamics of this model for $\hbar\omega_1, \hbar\omega_2 \ll U, E$; in this regime, the dipole Hamiltonian given by Eq. 5 may be used to describe the dynamics of the bosons. In what follows, we shall make the electric field E and the hopping J time dependent according to the protocol

$$\begin{aligned} E(t) &= U - E_0 \cos(\omega_1 t) \\ J(t) &= J_0 \left(1 + \cos(r\omega_1 t)\right) \end{aligned} \tag{31}$$

with $J(0) = 1$. The electric field E may be made time-dependent by varying the Zeeman field used to generate it as a function of time[38] while the detailed method creating a time dependent J in realistic experimental situation has been discussed in Ref. 40. Following the convention used in previous studies on this model, we shall choose $U/J(0) = 40$, $E_0/J(0) = 10$ and $n_0 = 1$ so that the dynamics takes the system through the critical point located $E_c = U + 1.83J$[34].

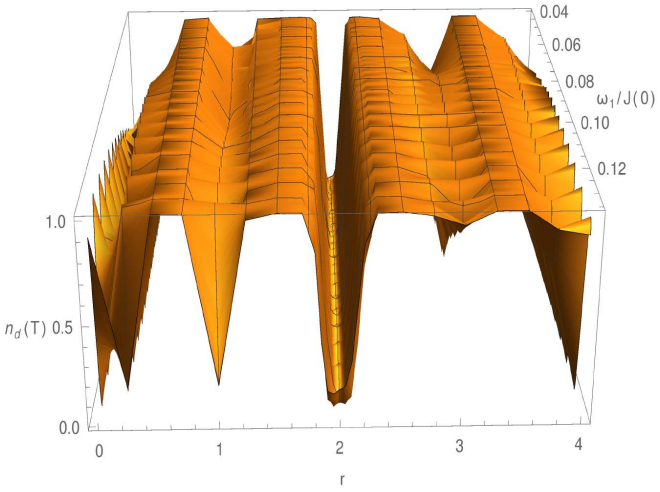

FIG. 6: Plot of the excitation density $n_d = 1 - F$ at $t = T$ as a function of ω_1 and r for $N = 12$, $E(0) = 30J(0)$ and $U = 40J(0)$. Note that $n_d \simeq 0$ for $r = 2$ independent of ω_1.

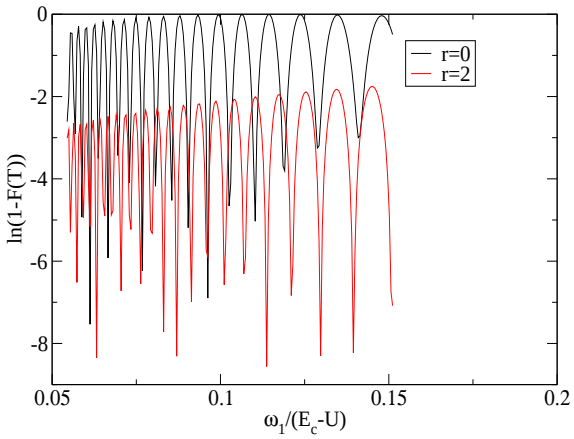

FIG. 7: Plot of $\ln(1 - F)$ as a function of ω_1 for $r = 0$ and 2 for $N = 14$. All other parameters are same as in Fig. 6.

To solve for the dynamics, we obtain the instantaneous eigenvalues and eigenvectors of the Hamiltonian H_d given by Eq. 5 with $J(t) = J(0)$ and $E(t) = E(0)$ using exact diagonalization (ED) for a bosonic chain with $N \leq 16$ sites. We denote these many-body states by $|m\rangle$; they satisfy $H_d[J(0), E(0)]|m\rangle = \epsilon_m|m\rangle$ with ϵ_1 and $|1\rangle$ being the ground state energy and wavefunction respectively. Having obtained $|m\rangle$, the wavefunction $|\psi(t)\rangle$ at any time which satisfies the Schrodinger equation $i\hbar\partial_t|\psi(t)\rangle = H_d[J(t), E(t)]|\psi(t)\rangle$, can be expressed as

$$|\psi(t)\rangle = \sum_m c_m(t)|m\rangle. \tag{32}$$

To obtain $c_m(t)$, we write the time-dependent Hamiltonian H_d at any instant as

$$\begin{aligned} & H_d[J(t), E(t)] = H_d[J(0), E(0)] - J_0\cos(r\omega_1 t) \\ & \times \sum_\ell (f_\ell + f_\ell^\dagger) + E_0(1 - \cos(\omega_1 t)) \sum_\ell n_\ell \qquad (33) \\ = \; & H_d[J(0), E(0)] - J_0\cos(r\omega_1 t)\Lambda_1 \\ & + E_0(1 - \cos(\omega_1 t))\Lambda_2. \end{aligned}$$

where the operators $\Lambda_{1,2}$ can be read off as $\Lambda_1 = \sum_\ell n_\ell$ and $\Lambda_2 = \sum_\ell (f_\ell + f_\ell^\dagger)$. Since $|m\rangle$ are eigenstates of $H_d[J(0), E(0)]$, this allows us to write

$$\begin{aligned} (i\hbar\partial_t - \epsilon_m)c_m \; = \; & \sum_p c_p \Big[E_0(1 - \cos(\omega_1 t))\langle m|\Lambda_2|p\rangle \\ & - J_0\cos(r\omega_1 t)\langle m|\Lambda_1|p\rangle \Big] \qquad (34) \end{aligned}$$

These equations are solved numerically for a chain of length $N \leq 16$ sites to obtain $c_m(t)$ and hence the wavefunction $|\psi(t)\rangle$. In our numerics, we find that all results have similar features for $10 \leq N \leq 16$. Keeping in mind that experimental realization of such systems typically involves $N \leq 12$, we present our numerical results for $16 \leq N \leq 12$. In what follows, we shall use $|\psi(t = T)\rangle$ to compute wavefunction overlap F, the excitation density n_d, and the dipole correlation functions $C_{\ell\ell'}$ which are given by

$$\begin{aligned} F \; &= \; |\langle\psi(T)|0\rangle|^2 = |c_0(T)|^2 = 1 - n_d \qquad (35) \\ C^d_{\ell\ell'} \; &= \; \langle\psi(T)|n_\ell n_{\ell'}|\psi(T)\rangle = \sum_{mp} c^*_m(T)c_p(T)\langle m|n_\ell n_{\ell'}|p\rangle \end{aligned}$$

The results that we obtain from the above mentioned analysis is shown in Fig. 6 showing variation of $n_d(T)$ as a function of ω_1 and r for $N = 12$. We find that for most r, n_d is an oscillating function of ω_1 which is qualitatively similar to its behavior for single rate drive protocols studied earlier[26]. However for $r = 2$, n_d displays a minimum for any ω_1; for $r = 2$, the value of n_d always ranges between 10^{-2} and 10^{-9}. This behavior can be clearly seen from Fig. 9 where $\ln(1 - F) = \ln n_d$ is plotted as a function of ω_1 with $N = 14$ and for $r = 0$ and $r = 2$. The plot shows that $\ln n_d \leq -2$ for any ω_1 when $r = 2$; thus for $r = 2$, the system displays dynamic freezing for a wide range of ω_1. We find numerically that the overlap between the final and the initial wavefunctions is closer to unity for $r = 2$ than for any other r and ω_1. We have checked that such dynamic freezing phenomenon is independent of the system size N within the range of N covered in our numerical analysis; n_d shows a dip at $r = 2$ for all $N \leq 16$.

To understand this phenomenon, we analyze the wavefunction overlap coefficients $|c_n(t)|^2$ as a function of time t for both $r = 0$ and $r = 2$. A plot of these coefficients is shown in Fig. 8 for $r = 0$ and $r = 2$. The plot shows that for $r = 0$, the system wavefunction $|\psi(t)\rangle$ has overlap with several eigenstates $|m\rangle$ (eigenstates of $H(0)$) as shown in left panel of Fig. 8. In particular, the change in overlap $|\psi(t)\rangle$ with $|m\rangle$ which

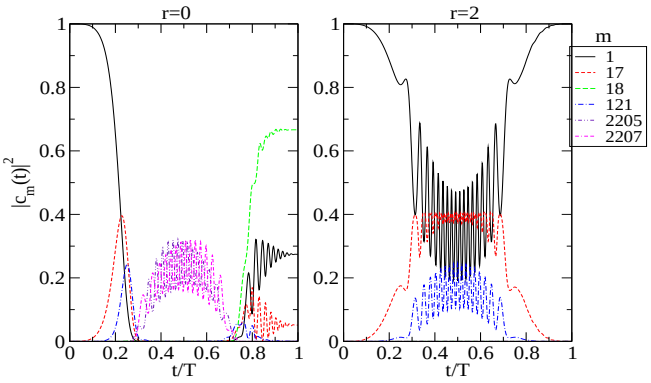

FIG. 8: Plot of the wavefunction overlap coefficients $|c_m(t)|^2$ as a function of t with $\omega_1/(E_c - U) = 0.107$ and $N = 16$ for (a) $r = 0$ and (b) $r = 2$. We have only plotted coefficients for which $|c_m(t)|^2 \geq 10^{-4}$. All other parameters are same as in Fig. 6.

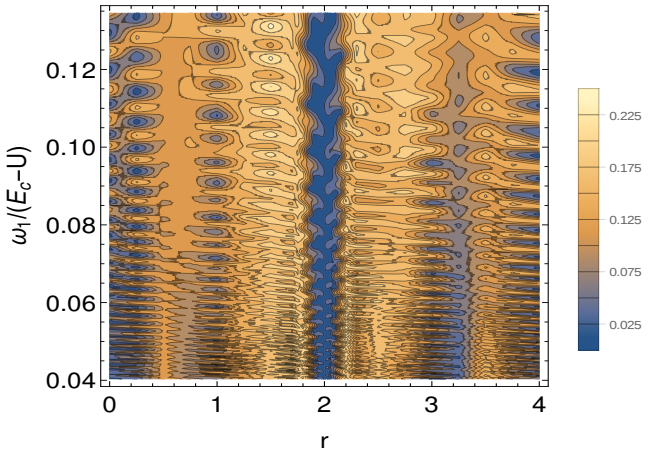

FIG. 9: Plot of the dipole correlation function $C_2^d(T)$ for $N = 12$ as a function of ω_1 and r showing absence of correlation at $r = 2$ for any ω_1. All parameters are same as in Fig. 6.

occur near $t \simeq T/4, 3T/4$ when the system traverses the critical point separating the dipole vacuum and maximal dipole ground states involves several $|m\rangle$ for $r = 0$. Also around these points at $r = 0$, J is finite which facilitates transfer of weight of $|\psi(t)\rangle$ between different $|m\rangle$ (since these are states with different average dipole numbers $\langle m|\sum_i n_i|m\rangle$); consequently, one does not expect the system to return to its initial ground state at $t = T$ for generic ω_1. In contrast, for $r = 2$, we find that very few states ($m = 1$, 121, and 2207) contribute to $|\psi(t)\rangle$. Moreover at $t = T/4, 3T/4$, the transfer of weights occur only between states $|m = 1\rangle$ (dipole vacuum ground state) and $|m = 2207\rangle$ (maximal dipole state for $N = 16$). Thus around these points, the dynamics is controlled by an effective two-level system similar to those analyzed in Sec. II. In addition, we note $J(t)$ vanishes at the critical point for $r = 2$ and remains very small around the critical point; thus these two levels undergo a nearly unavoided level crossing at $t = T/4, 3T/4$ since the matrix element of $H(t)$ between states with different dipole number is extremely small when $J(t) \simeq 0$. This feature, together with the fact only these two states are involved in dynamics of the system, ensures that $|c_1(t = T)|^2 \simeq 1$ which leads to dynamic freezing. The degree of this overlap depends on ω_1; however since $J(t)$ always vanishes at $t = T/4, 3T/4$, the overlap is always close to unity leading to $\ln(1 - F) \leq -2$ for the entire range of ω_1 studied in our numerics.

Finally, we plot the dipole correlation function between sites $\ell = 2$ and $\ell' = 0$, $C_{20}^d(T) \equiv C_2^d(T)$, as a function of r and ω_1 in Fig. 9. The choice of the site indices are motivated as follows. Due to the constraint $n_\ell \leq 1$ and $n_\ell n_{\ell+1} = 0$ on the dipole Hamiltonian, $\langle n_\ell^2\rangle = \langle n_\ell\rangle$ and $\langle n_\ell n_{\ell+1}\rangle = 0$ for any ℓ. Thus the first non-trivial correlation between dipoles occur for $|\ell - \ell'| = 2$. We find that $C_2^d(T)$ is generically an oscillating function of ω_1 for any r expect at $r = 2$ where its close to zero for all ω_1. This behavior can be understood from the fact at $r = 2$, $|\psi(t)\rangle$ is close to the starting ground state $|m = 1\rangle$. Since we start our dynamics in a parameter regime where the ground state is dipole vacuum, $|m = 1\rangle$ and hence $|\psi(t)\rangle$ has no dipole correlations.

IV. DISCUSSION

In this work, we have studied periodic dynamics of a class of integrable [represented by free fermionic Hamiltonian (Eq. 1)] and an experimentally realizable non-integrable model [represented by bosonic Hamiltonian (Eq. 5)] using a two-rate protocol. For numerical purposes, we have chosen the 1D XY model in a transverse field as a representative example of the class of integrable model. For each of these models, we find that the second drive frequency $\omega_2 = r\omega_1$ can act as tuning knob to achieve dynamical freezing.

For integrable models represented by Eq. 1, we obtain a semi-analytic expression for the wavefunction at the end of a drive cycle within the adiabatic-impulse approximation. Our results constitute a generalization of this method for application to integrable systems driven by arbitrary two-rate protocols. We compare the results obtained by this method, for low-enough drive frequencies where it is expected to be accurate, to exact numerics and find almost exact match between the two. Our numerics, for these integrable models, also reveal that the dynamics at $r = 1$ is qualitatively different from those of $r \neq 1$; for $r = 1$, dynamic freezing is obtained for a wide range of ω_1. This behavior can be analytically explained at a qualitative level. We also show that the signature of such dynamic freezing can be easily deduced from fermionic correlators (or equivalently transverse magnetization of the XY model); the change in magnetization shows a near zero value at $r = 1$ for a wide range of ω_1.

For the tilted Bose-Hubbard model, we drive the applied electric field and the hopping parameter as a function of time with frequencies ω_1 and $\omega_2 = r\omega_1$ respectively. We find, similar to integrable models discussed earlier, that r may act as a tuning parameter for obtaining dynamical freezing;

for our protocol choice, we find that for $r = 2$ the system undergoes dynamic freezing for a wide range of ω_1. We show that for $r = 2$, the wavefunction overlap F satisfies $-2 \geq \ln(1-F) \geq -9$ which constitutes a much better overlap between the final and the initial wavefunction than what can be achieved in single-rate protocols[26]. We provide a semi-analytic justification of such near-perfect dynamic freezing and discuss its signature in dipole-dipole correlation function.

Experimental verification of our result could be most easily achieved by on-site parity of boson occupation ($(-1)^{n_i}$) measurement of bosons in the tilted Bose Hubbard model after a drive cycle. Such measurement have already been carried out for tilted bosons in equilibrium for $N = 12$ sites[38]. Here we propose to start from the dipole vacuum ($n_d = 0$) state which correspond to odd ($n = 1$) boson occupation on all sites. We then propose to drive the system for one full period using the two-rate protocol given by Eq. 31 and measure the number of sites with even bosons. Since formation of a dipole in this case always lead to even ($n = 0, 2$) boson occupation at adjacent sites, such a measurement provide us with information on dipole density and hence $1 - F$. We predict that for $r = 2$, almost no dipoles would be created for a wide range of ω_1.

In conclusion, we have studied two-rate periodic protocols applied to a class of integrable models and an experimentally realizable non-integrable models. Our study reveals that the second drive frequency may be used as a tuning parameter to achieve dynamical freezing. We have provided a detailed analysis of this phenomenon, analyzed their signature in correlation functions, and suggested concrete experiments to test our theory.

Acknowledgement: KS thanks J.D. Sau for discussion on related projects. SK acknowledges financial support from CSIR, India, under Scientists' Pool Scheme No. 13(8764-A)/2015-Pool.

[1] A. Polkovnikov, K. Sengupta, A. Silva, and M. Vengalattore, Rev. Mod. Phys., **83**, 863 (2011).

[2] J. Dziarmaga, Adv. Phys. **59**, 1063 (2010).

[3] A. Dutta, U. Divakaran, D. Sen, B. K. Chakrabarti, T. F. Rosenbaum, and G. Aeppli, arXiv:1012.0653 (unpublished).

[4] T. W. B. Kibble, J. Phys. A **9**, 1387 (1976); W. H. Zurek, Nature (London) **317**, 505 (1985).

[5] A. Polkovnikov, Phys. Rev. B **72**, 161201(R) (2005).

[6] K. Sengupta, D. Sen and S. Mondal, Phys. Rev. Lett. **100**, 077204 (2008).

[7] D. Sen, K. Sengupta and S. Mondal, Phys. Rev. Lett. **101**, 016806 (2008).

[8] A. Polkovnikov, Phys. Rev. Lett. **101**, 220402 (2008).

[9] A. Chandran, A. Erez, S. S. Gubser, and S. L. Sondhi, Phys. Rev. B **86**, 064304 (2012).

[10] F. Pollmann, S. Mukerjee, A. M. Turner, and J. E. Moore Phys. Rev. Lett. **102** 255701 (2009).

[11] M. Heyl, A. Polkovnikov, and S. Kehrein Phys. Rev. Lett. **110**, 135704 (2013).

[12] C. Karrasch and D. Schuricht, Phys. Rev. B, **87**, 195104 (2013); N. Kriel, C. Karrasch, and S. Kehrein Phys. Rev. B **90**, 125106 (2014)

[13] F. Andraschko, J. Sirker, Phys. Rev. B **89**, 125120 (2014); E. Canovi, P. Werner, and M. Eckstein, Phys. Rev. Lett. **113**, 265702 (2014); M. Heyl, Phys. Rev. Lett. **115**, 140602 (2015).

[14] S. Sharma, U. Divakaran, A. Polkovnikov, and A. Dutta, arXiv:1601.01637 (unpublished).

[15] L. M. Sieberer, S. D. Huber, E. Altman, and S. Diehl, Phys. Rev. Lett. **110**, 195301 (2013).

[16] S. de Sarkar, R. Sensarma, and K. Sengupta, Jour. Phys. Cond. Mat., **23**, 305602 (2014).

[17] A. Mitra and T. Giamarchi, Phys. Rev. Lett. **107** 150602 (2011); A. Mitra and T. Giamarchi, Phys. Rev. B **85** 075117 (2012).

[18] E. C. G. Stuckelberg, Helv. Phys. Acta **5**, 369 (1932).

[19] M. Demirplak and S. A. Rice, J. Chem. Phys. A **107**, 9937 (2003); *ibid*, J. Chem. Phys. B **109**, 6838 (2005).

[20] W. D. Oliver, Y. Yu, J. C. Lee, K. K. Berggren, L. S. Levitov, and T. P. Orlando, Science **310**, 1653 (2005); M. S. Rudner, A. V. Shytov, L. S. Levitov, D. M. Berns, W. D. Oliver, S. O. Valenzuela, T. P. Orlando, Phys. Rev. Lett. **101**, 190502 (2008)

[21] A. Das, Phys. Rev. B, **82**, 172402 (2010); S. Hegde, H. Katiyar, T. S. Mahesh, and A. Das, Phys. Rev. B **90**, 174407 (2014).

[22] A. del Campo and K. Sengupta, Eur. Phys. Jour. Sp. Topics, **224**, 189 (2015)

[23] A. Dutta, A. Das, and K. Sengupta, Phys. Rev. E **92**, 012104 (2015).

[24] A. Sen, and K. Sengupta, arXiv:1511.03668 (unpublished).

[25] S. Mondal, D. Pekker and K. Sengupta EuroPhys. Lett. **100**, 60007 (2012).

[26] U. Divakaran, and K. Sengupta, Phys. Rev. B **90**, 184303 (2014).

[27] J. D. Sau and K. Sengupta, Phys. Rev. B **90**, 104306 (2014).

[28] S. Sachdev, *Quantum Phase Transitions* (Cambridge University Press, Cambridge, England, 1999).

[29] A. Kitaev, Ann. Phys. (NY) **321**, 2 (2006);

[30] D. Sen, K. Sengupta, and S.Mondal, Phys.Rev. Lett **101**, 016806 (2008).

[31] X.-Y. Feng, G.-M. Zhang, and T. Xiang, Phys. Rev. Lett. **98**, 087204 (2007).

[32] A. H. Castro Neto, F. Guinea, N. M. R. Peres, K. S. Novoselov, and A. K. Geim, Rev. Mod. Phys. **81**, 109 (2009); S. Das Sarma, S. Adam, E. H. Hwang, and E. Rossi, Rev. Mod. Phys. **83**, 407 (2011); M. O. Goerbig, Rev. Mod. Phys. **83**, 1193 (2011); D. N. Basov, M.M. Fogler, A. Lanzara, F.Wang, and Y. Zhang, Rev. Mod. Phys. **86**, 959 (2014).

[33] M. Z. Hasan and C. L. Kane Rev. Mod. Phys. **82**, 3045 (2010);X-L Qi and S-C Zhang, Rev. Mod. Phys. **83**, 1057 (2011).

[34] S. Sachdev, K. Sengupta, and S. M. Girvin, Phys. Rev. B **66**, 075128 (2002).

[35] S. Pielawa, T. Kitagawa, E. Berg, and S. Sachdev, Phys. Rev. B **83**, 205135 (2011); S. Pielawa, E. Berg, and S. Sachdev, Phys. Rev. B **86**, 184435 (2012)

[36] K. Sengupta, S. Powell, and S. Sachdev, Phys. Rev.A **69**, 053616 (2004).

[37] M. Kolodrubetz, D. Pekker, B. K. Clark, and K. Sengupta, Phys. Rev. B **85**, 100505 (2012).

[38] J. Simon, W. Bakr, R. Ma, M. E. Tai, P. Preiss, and M. Greiner, Nature (London) **472**, 307 (2011).

[39] S. N. Shevchenko, S. Ashhab, and F. Nori, Phys. Rep. **492**, 1 (2010).

[40] S. de Sarkar, R. Sensarma, and K. Sengupta, Phys. Rev. B **92**, 174529 (2015).